LECTURE NOTES IN COMPUTATIONAL SCIENCE AND ENGINEERING 143

Vladimir A. Garanzha
Lennard Kamenski · Hang Si *Editors*

Numerical Geometry, Grid Generation and Scientific Computing

Springer

Adaptive Grids for Non-monotone Waves and Instabilities in a Non-equilibrium PDE Model

Paul A. Zegeling

Abstract In this paper, the importance of both the analysis and computation is emphasized, in relation to a bifurcation problem in a non-equilibrium Richard's equation from hydrology. The extension of this PDE model for the water saturation S, to take into account additional dynamic memory effects gives rise to an extra third-order mixed space-time derivative term in the PDE of the form $\tau\ \nabla \cdot [f(S)\nabla(S_t)]$. In one space dimension, travelling wave analysis is able to predict the formation of steep non-monotone waves depending on the parameter τ. In two space dimensions, the parameters τ and the frequency ω of a small perturbation term, predict that the waves may become *unstable*, thereby initiating so-called gravity-driven fingering structures. For the numerical experiments of the time-dependent PDE model, we have used a sophisticated adaptive grid r-refinement technique based on a scaled monitor function.

1 Introduction

Space-time evolution described by nonlinear PDE models involves patterns and qualitative changes induced by parameters. In this report I will emphasize the importance of both the analysis and computation in relation to a bifurcation problem in a non-equilibrium Richard's equation from hydrology. The extension of this PDE model for the water saturation S, to take into account additional dynamic memory effects, was suggested by Hassanizadeh and Gray [7] in the nineties of the last century. This gives rise to an extra third-order mixed space-time derivative term in the PDE of the form $\tau\ \nabla \cdot [f(S)\nabla(S_t)]$. In one space dimension, travelling wave analysis is able to predict the formation of steep non-monotone waves depending on the parameter τ. It is shown that, in this framework, theory from applied analysis, accurate numerical PDE solutions and also the experimental observations from the

P. A. Zegeling (✉)
Utrecht University, Utrecht, The Netherlands
e-mail: P.A.Zegeling@uu.nl

V. A. Garanzha et al. (eds.), *Numerical Geometry, Grid Generation and Scientific Computing*, Lecture Notes in Computational Science and Engineering 143,
https://doi.org/10.1007/978-3-030-76798-3_11

laboratory [5, 14] can be nicely matched. In two space dimensions, the parameters τ and the frequency ω (appearing in a small perturbation term), predict that the waves may become *unstable*, thereby initiating so-called gravity-driven fingering structures. This phenomenon can be analysed with a linear stability analysis and its effects are supported by the numerical experiments of the 2D time-dependent PDE model. For this purpose, we have used an efficient adaptive grid r-refinement technique based on a scaled monitor function. The numerical experiments in one and two space dimensions confirm the theoretical predictions and show the effectiveness of the adaptive grid solver.

2 The Non-equilibrium PDE Model

The PDE model describing non-equilibrium effects in a two-phase porous medium is given by [4, 7–9, 21, 22]:

$$S_t = \nabla \cdot (\mathcal{D}(S)\nabla S) + [f(S)]_z + \tau \nabla \cdot [f(S)\nabla(S_t)],$$
$$\text{with} \quad (x, z, t) \in [x_L, x_R] \times [z_L, z_R] \times (0, T], \tag{1}$$

where τ is a non-equilibrium parameter, $\mathcal{D}(S)$ is a nonlinear diffusion function and $f(S)$ is a fractional flow function, respectively.

2.1 *The One-Dimensional Case*

Assuming a constant diffusion and a linearized non-equilibrium term, respectively, in one space dimension, PDE model (1) can be reduced to:

$$S_t = \mathcal{D}\, S_{zz} + [f(S)]_z + \tau S_{zzt}, \quad (z, t) \in [z_L, z_R] \times (0, T], \tag{2}$$

with initial condition $S(z, 0) = S_0(z)$. The water saturation is represented by the variable $S(z, t) \in [0, 1]$, $\mathcal{D} > 0$ is a diffusion coefficient and $\tau \geq 0$ the non-equilibrium parameter (see also [7, 21, 22]). The function f satisfies: $f(0) = 0, f(1) = 1, f'(S) > 0$ and is related to a fractional flow function in the porous media model [22]. In particular, two choices for the function f are considered. The first one is a convex-shaped function, representing a one phase situation (only water), i.e.,

$$f(S) = \frac{S^2}{2},$$

and the second one is a convex-concave function, indicating two phases (both water and air are present):

$$f(S) = \frac{S^2}{S^2 + (1-S)^2}.$$

Dirichlet conditions are imposed at the spatial boundaries: $S(z_L, t) = S_-$ and $S(z_R, t) = S_+$. The initial water saturation $S_0(z)$, the boundaries of the spatial domain, the final time T and the values for $0 \leq S_- < S_+ \leq 1$, $\mathcal{D}$ and τ will be specified in the description of the numerical experiments.

2.2 *Travelling Waves: A Bifurcation Diagram*

This section discusses special types of solutions in PDE model (2): we are interested in travelling wave (TW) solutions. For simplicity of the analysis, we assume that $f(S) = S^2$. The convex-concave case is treated in [21, 22] which gives rise to an even richer structure of the dynamics. The TW Ansatz, assuming a positive constant speed ν, can be written as:

$$S(z,t) = \varphi(z + \nu\, t) := \varphi(\zeta), \quad \zeta \in (-\infty, +\infty), \quad \nu > 0.$$

Substituting this Ansatz in PDE (2), yields the third-order ODE:

$$\nu\, \varphi' = \mathcal{D}\, \varphi'' + [\varphi^2]' + \nu\, \tau\, \varphi''', \tag{3}$$

where the $'$ stands for taking derivatives with respect to the TW-variable ζ. Integrating (3) between $-\infty$ and ζ and using the fact that $\varphi(-\infty) = S_-, \varphi'(-\infty) = \varphi''(-\infty) = 0$, gives the second-order ODE:

$$\nu\, (\varphi - S_-) = \mathcal{D}\, \varphi' + \varphi^2 - S_-^2 + \nu\, \tau\, \varphi'', \tag{4}$$

which can be re-written as a system of first-order ODEs:

$$\begin{cases} \varphi' = \psi, \\ \psi' = \frac{\nu(\varphi - S_-) + S_-^2 - \varphi^2 - \mathcal{D}\, \psi}{\nu\, \tau}. \end{cases} \tag{5}$$

A TW for (2) in the coordinate system (x, t) is represented by a trajectory in the (φ, ψ)-plane connecting an unstable stationary point (at $\zeta = -\infty$) of (5) with a stable one (at $\zeta = +\infty$). There are only two stationary points in system (5):

$(\varphi, \psi) = (S_-, 0)$, and $(\varphi, \psi) = (S_+, 0)$. The eigenvalues of the linearized system of (5) can easily be calculated:

$$\lambda_{1,2} = \frac{-\mathcal{D}}{2\tau v} \pm \sqrt{\frac{\mathcal{D}^2}{4\tau^2 v^2} + \frac{S_+ - S_-}{2\tau v}}. \tag{6}$$

From (6) it follows that the point $(S_-, 0)$ is an unstable (saddle) point in all cases, since $\lambda_1 \lambda_2 < 0$. Depending on the PDE parameters $\mathcal{D}$ and τ, we distinguish between two cases for the second stationary point $(S_+, 0)$. Non-monotone TWs exist for $\tau > \tau_c = \mathcal{D}^2/(S_+ - S_-)$ since the saddle point is then connected to a spiral point (a focus). This situation is clarified in terms of the PDE solutions (Fig. 1), a bifurcation diagram (left panel in Fig. 2) and a phase plane plot (right panel in Fig. 2). For $\tau = 0$, it is known that only monotone waves satisfy the PDE model [4]. Since we are looking also for non-monotone waves, we need the extra τ-term in PDE (2) to describe such phenomena. Note again that the convex-concave case is treated in [22], for which there may exist *plateau-type* waves as well. In that case three stationary points appear in the dynamical system with a much more complicated behaviour in the phase plane. These plateau-waves will be detected in

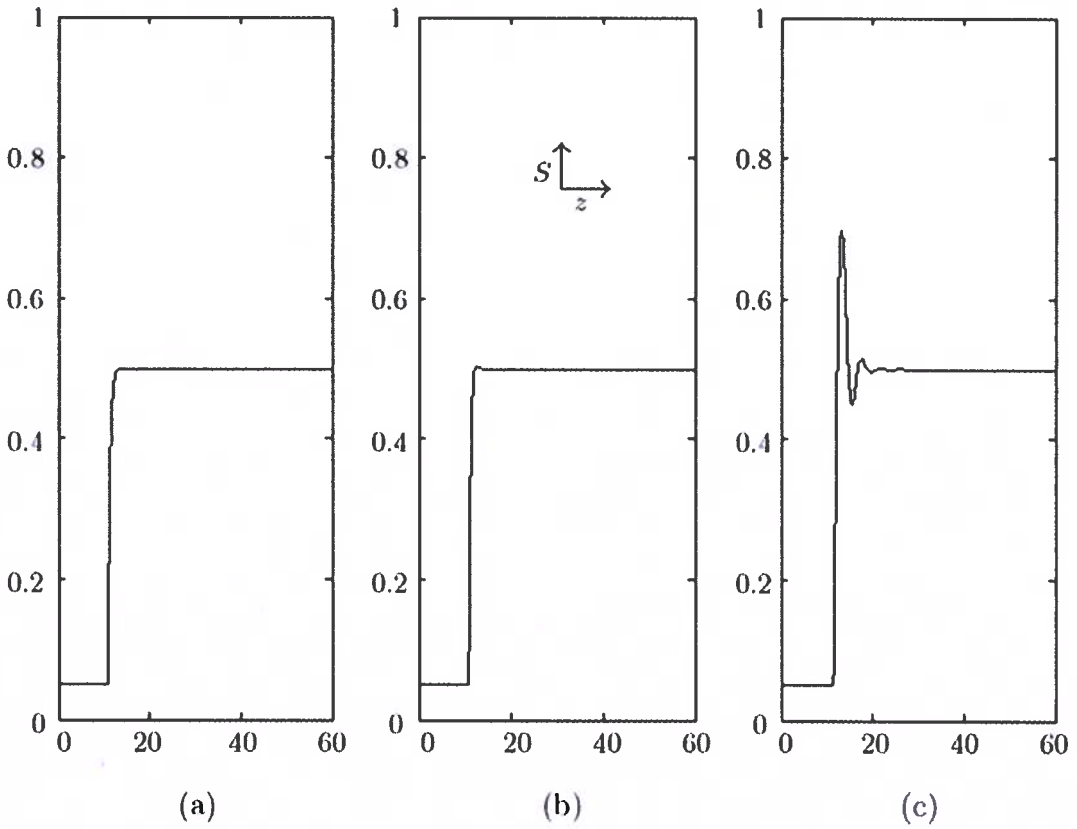

Fig. 1 The one-dimensional saturation profile for various values of the non-equilibrium parameter τ: (**a**) $\tau = 0$ (monotone TW); (**b**) $\tau = 1$ (mildly non-monotone TW); (**c**) $\tau = 5$ (oscillating non-monotone TW)

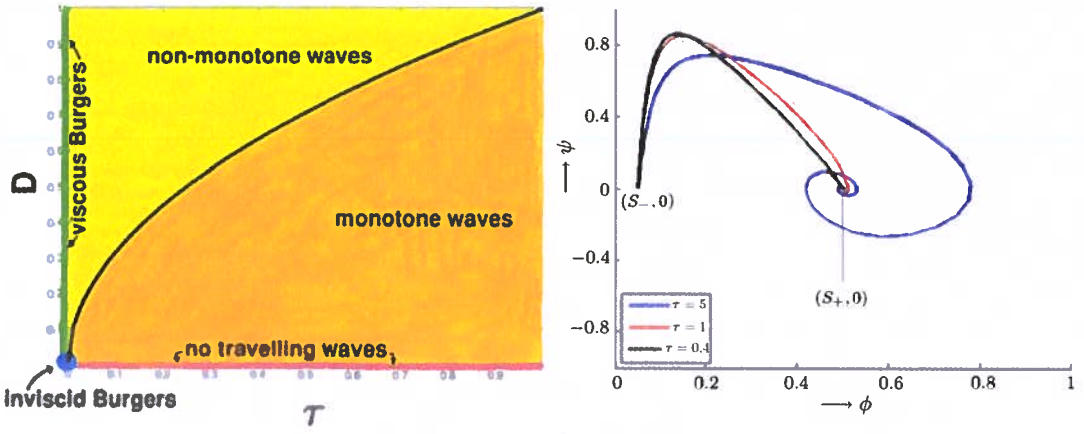

Fig. 2 A bifurcation diagram (left) indicating the existence of monotone waves and non-monotone waves depending on the parameters $\mathcal{D}$ and τ. The black curve is defined by: $\mathcal{D} = \sqrt{\tau(S_+ - S_-)}$. The right panel shows, for three different values of the parameter τ, trajectories in the phase plane (φ, ψ). The red and blue curves correspond to non-monotone waves ($\tau > \tau_c > 0$) and the black curve denotes a monotone wave ($\tau = 0$)

the numerical experiments, where we will use an adaptive moving grid method to solve the PDE model (2).

2.3 *The Adaptive Moving Grid in 1D*

For the numerical simulations of PDE model (2) we will apply an adaptive moving grid technique that is based on a coordinate transformation (for more details: [2, 8, 10, 11, 19, 24, 25]):

$$\begin{cases} z = z(\xi, \vartheta), \\ t = t(\xi, \vartheta) = \vartheta. \end{cases} \tag{7}$$

Then, PDE model (2) is transformed to the following form:

$$\upsilon_\vartheta - \frac{(\upsilon + z_\vartheta)}{\mathcal{J}}\upsilon_\xi = \frac{\mathcal{D}}{\mathcal{J}}\left(\frac{\upsilon_\xi}{\mathcal{J}}\right)_\xi + \frac{\upsilon_\xi}{\mathcal{J}} f'(\upsilon) + \frac{\tau}{\mathcal{J}}\left[\mathcal{J}\left(\frac{1}{\mathcal{J}}\left(\frac{\upsilon_\xi}{\mathcal{J}}\right)_\xi\right)_\vartheta - z_\vartheta\left(\frac{1}{\mathcal{J}}\left(\frac{\upsilon_\xi}{\mathcal{J}}\right)_\xi\right)_\xi\right], \tag{8}$$

with $v(\xi,\vartheta) := S(z(\xi,\vartheta),\vartheta)$ and the Jacobian of transformation (7): $\mathcal{J} := z_\xi$. The adaptive grid transformation that defines the time-dependent non-uniform grid has to satisfy the adaptive grid PDE;

$$[(\sigma(\mathcal{J}) + \tau_s\,\mathcal{J}_\vartheta)\,\mathcal{M}]_\xi = 0, \quad \tau_s \geq 0.$$

Here, $\mathcal{M} := \sqrt{1+[S_z]^2}$ is the monitor function, reflecting the dependence of the non-uniform grid on the spatial derivative of the PDE solution.

The operator

$$\sigma := \mathcal{I} + \kappa_s(\kappa_s+1)\frac{\partial^2}{\partial\xi^2}$$

is applied to obtain a smoother grid transformation in space. The first adaptivity constant $\kappa_s > 0$ is a spatial smoothing (or filtering) parameter. Further, the second adaptivity constant τ_s takes care of the smoothness in the time-direction. For $\kappa_s > 0$ and $\tau_s > 0$, after semi-discretization, it can be shown [10] that the spatial grid satisfies the condition

$$\frac{\kappa_s}{\kappa_s+1} \leq \frac{\Delta z_{i+1}}{\Delta z_i} \leq \frac{\kappa_s+1}{\kappa_s}$$

for all gridpoints z_i and all time $t > 0$. Note that, for $\kappa_s = \tau_s = 0$ (no smoothing), we return to the basic equidistribution principle $[z_\xi \mathcal{M}]_\xi = 0$. For more details on the adaptive grid and the smoothing operators we refer to [10, 24, 25]. The transformed PDE and the adaptive grid PDE are simultaneously semi-discretized in the spatial direction following a method-of-lines approach. A central, second-order, uniform approximation for the transformed derivative terms in the ξ-direction is used. The time-integration of the resulting coupled ODE-system is done by a BDF method with variable time-steps in DASSL [16].

2.4 *Numerical Results*

In this section, we perform some numerical experiments to show the accuracy and effectiveness of the adaptive moving grid. This will also illustrate and confirm the TW analysis in Sect. 2.2. The adaptive grid parameters are chosen as follows: $\kappa_s = 2$ and $\tau_s = 0.001$ and the time-integration a tolerance in DASSL is set to the value 10^{-4}. The initial condition is a steep wave starting at the right boundary of the domain and reads:

$$S(z,0) = S_0(z) = S_- + \frac{1}{2}(S_+ - S_-)(1+\tanh(R(z-z_0))),$$

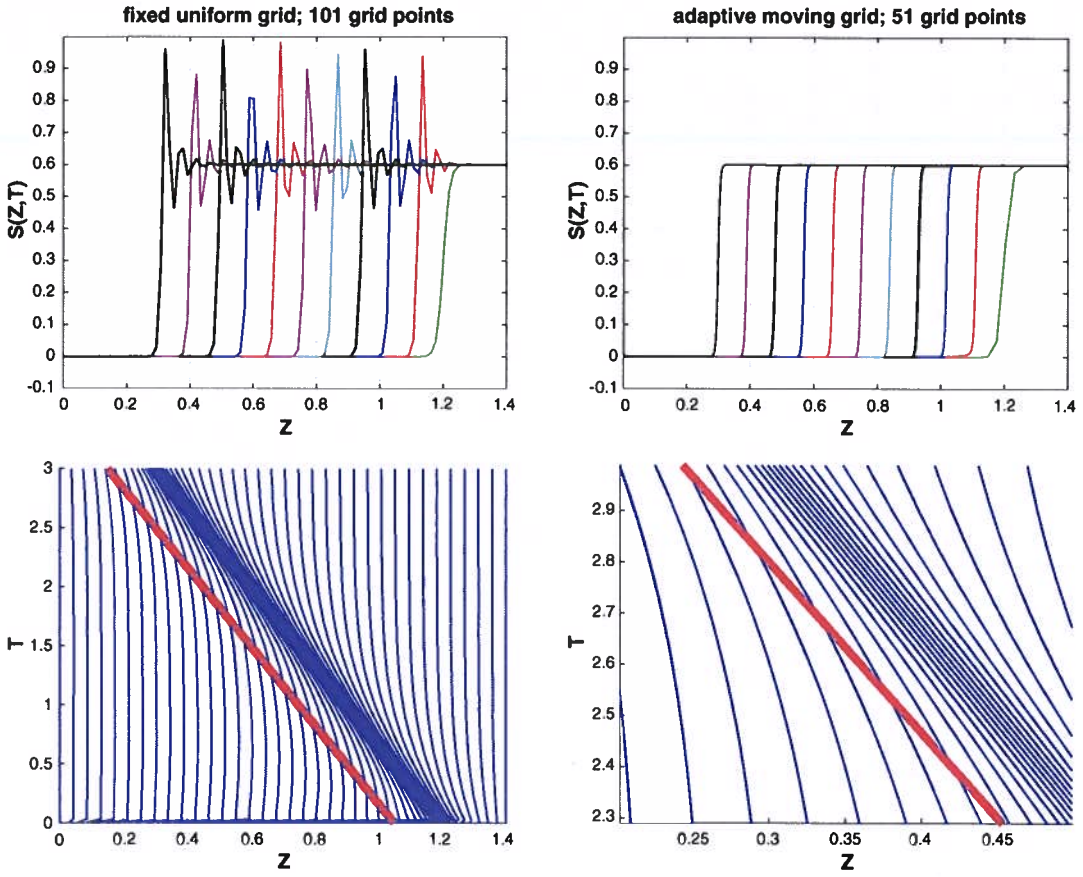

Fig. 3 Upper two panels for the case $\tau = 0$: oscillating uniform ($N = 101$) grid solutions (left) and non-oscillating adaptive grid solutions with $N = 51$ (right). The lower two plots (with a close-up in the right panel) display the time-history of the adaptive grid. In these experiments, we have chosen: $\tau = 3 \times 10^{-4}$, $\mathcal{D} = 2 \times 10^{-3}$. The red lines indicate the exact (asymptotic) wave speed

where $z_L = 0$, $z_R = 1.4$, $S_- = 0$, $S_+ = 0.6$, $R = 50$ and PDE parameters: $\tau = 10^{-4}$ and $\mathcal{D} = 10^{-3}$. In Fig. 3 we show, for $\tau = 0$, in which case we know that only monotone solutions exist, numerical solutions with $N = 101$ fixed uniform grid points and with $N = 51$ adaptive moving grid points. It is clearly observed that the uniform grid produces an unwanted non-monotone wave, whereas the adaptive grid nicely keeps the wave monotone. Also, the plot with the time history of the adaptive grid illustrates the smooth distribution and time-behaviour of the grid with a constant wave velocity. Figure 4 displays the difference between the convex and the convex-concave case: non-monotone TWs and plateau-waves. These waves are predicted by the analysis in Sect. 2.2 and [22].

From ODE (4) it can easily be derived that the asymptotic travelling-wave speed v satisfies:

$$v = \frac{f(S_+) - f(S_-)}{S_+ - S_-}. \tag{9}$$

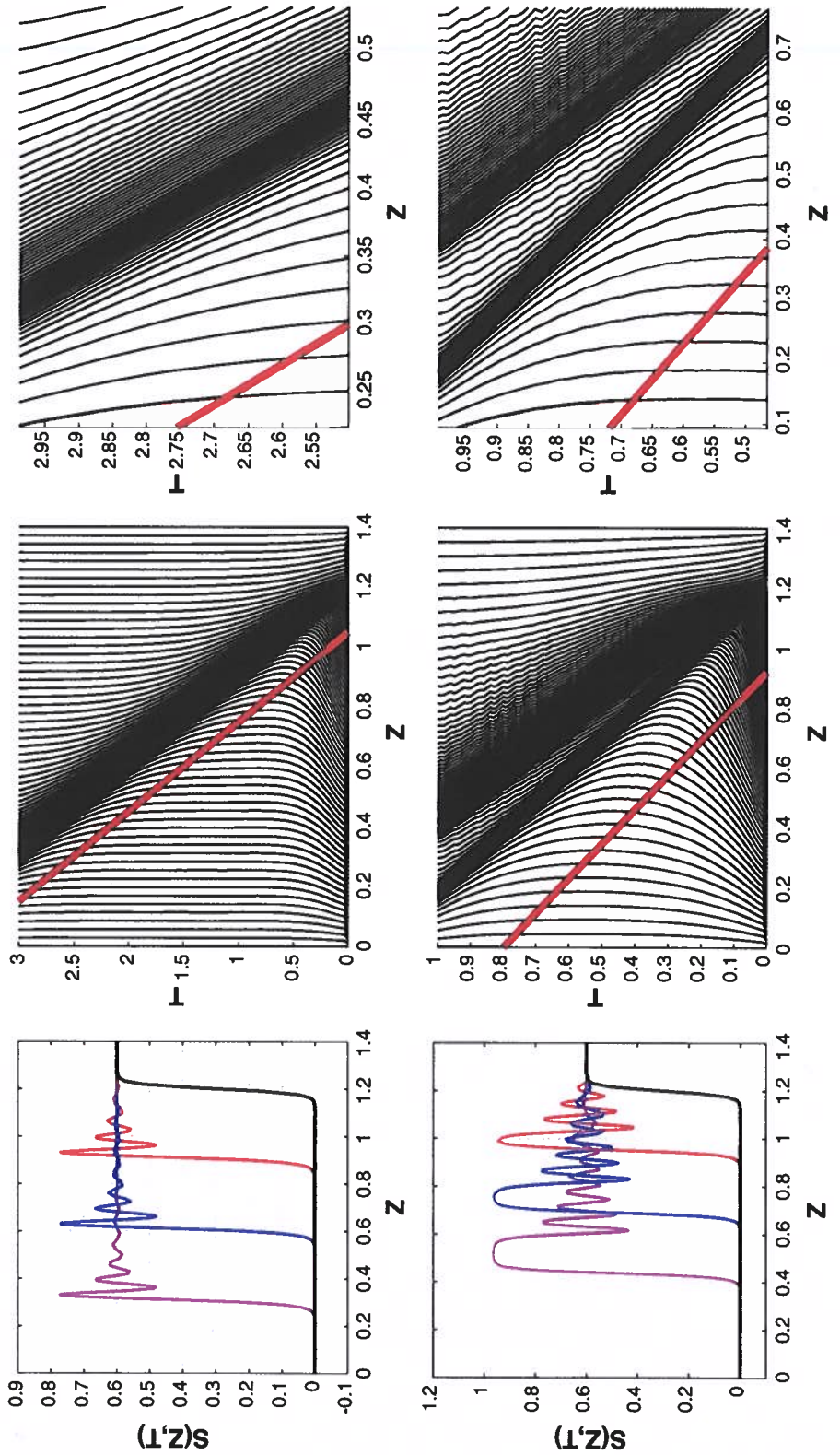

Fig. 4 The time history of the adaptive grid (right, with a close-up around the steep parts of the waves), the solutions at four points of time (left) for two characteristic cases in the porous media model: a convex f (top) and a convex-concave f (bottom). The red straight lines indicate the exact (asymptotic) wave speeds for the two cases, as predicted by formula (9)

This yields, respectively, for the convex case $\nu = 0.3$ and for the convex-concave case $\nu \approx 1.1538$. In Figs. 3 and 4 the red lines indicate these constant TW speeds. We observe that the adaptive moving grid follows the waves very accurately.

3 The Two-Dimensional Case

Next, we consider the two-dimensional version of model (1) for the special choices:

$$f(S) = S^{\alpha}, \quad \mathcal{D}(S) = \beta S^{\alpha-\beta-1}, \quad \alpha > \beta + 1. \tag{10}$$

3.1 Non-monotone Waves and Instabilities

In contrast with the 1D case, for which both the monotone and non-monotone waves are stable under small perturbations, the 2D model may give rise to *in*stabilities ('finger' structures). It can be shown that for specific values of $\tau > 0$, the non-monotone waves may become *un*stable. The analysis is based on the following observations, also mentioned in [6] and [15].

First, the non-equilibrium PDE (1) is re-written as a system of two equations, one for the saturation S and one for the pressure p:

$$\begin{cases} S_t = \nabla \cdot (\mathcal{D}(S)\nabla p) + [f(S)]_z, \\ \tau S_t = p - \mathcal{P}(S), \end{cases} \tag{11}$$

where $\mathcal{P}(S)$ is an equilibrium pressure. Next, the PDEs are written in a travelling wave coordinate, similar as in done in Sect. 2.2. The saturation and pressure waves are then perturbed in the following form:

$$\begin{cases} S = S_0(\zeta) + \varepsilon e^{i\omega_x + i\omega_z + kt} S_1(\zeta) + O(\varepsilon^2), \\ p = p_0(\zeta) + \varepsilon e^{i\omega_x + i\omega_z + kt} p_1(\zeta) + O(\varepsilon^2). \end{cases} \tag{12}$$

These perturbed quantities are substituted in the system of two travelling wave equations, higher-order terms are being neglected, and equations for the linear stability analysis are set up. For these, it can be derived, that, for $\tau = 0$, the growth factor k will always be negative, whereas, for $\tau > 0$ and for certain frequencies ω, the growth factor can be positive, thereby initiating unstable waves. These can be related to so-called fingering structures, as we will see in Sect. 3.3.

3.2 The Adaptive Moving Grid in 2D

The adaptive grid method in two dimensions follows similar principles, with some extra features and differences, compared to the 1D situation. More details can be found in, for example, the references [10, 18–20], and [23]. Summarizing the procedure, the 2D grid transformation reads:

$$\begin{cases} x = z(\xi, \eta, \vartheta), \\ z = z(\xi, \eta, \vartheta), \\ t = t(\xi, \eta, \vartheta) = \vartheta. \end{cases} \tag{13}$$

As an example, the first term of the nonlinear diffusion on the righthand side in PDE model (1) transforms to:

$$\begin{aligned} (\mathcal{D}(S)S_x)_x = \frac{1}{\mathcal{J}} \Bigg[& \left(\frac{\mathcal{D}(S) z_\eta^2}{\mathcal{J}} S_\xi \right)_\xi - \left(\frac{\mathcal{D}(S) z_\xi z_\eta}{\mathcal{J}} S_\eta \right)_\xi \\ & - \left(\frac{\mathcal{D}(S) z_\xi z_\eta}{\mathcal{J}} S_\xi \right)_\eta + \left(\frac{\mathcal{D}(S) z_\xi^2}{\mathcal{J}} S_\eta \right)_\eta \Bigg], \end{aligned} \tag{14}$$

where $\mathcal{J} = x_\xi z_\eta - x_\eta z_\xi$ denotes the determinant of the Jacobian of transformation (13). The one-dimensional basic equidistribution principle, $[\mathcal{M} z_\xi]_\xi = 0$, is extended to a system of two coupled nonlinear elliptic PDEs:

$$\begin{cases} \nabla \cdot (\mathcal{M} \nabla x) = 0, \quad \nabla := \left[\frac{\partial}{\partial \xi}, \frac{\partial}{\partial \eta} \right]^T, \\ \nabla \cdot (\mathcal{M} \nabla z) = 0, \end{cases}$$

where the monitor function $\mathcal{M}$ is now defined by

$$\mathcal{M} = \gamma(t) + \sqrt{\nabla S \cdot \nabla S}, \quad \text{with} \quad \gamma(t) = \iint_{\Omega_c} \sqrt{\nabla S \cdot \nabla S} \, \mathrm{d}\xi \, \mathrm{d}\eta \, .$$

It is obvious that more sophisticated monitor functions could be used, but, for the PDE model in this paper, this relatively simple monitor function has shown to be sufficiently effective. Note that we have added a time-dependent adaptivity function $\gamma(t)$ which is automatically calculated during the time-integration process. It provides additional smoothing to the grid distribution and takes care of the scaling in the space and solution directions (see [20] for more information about this choice). It can be shown that the adaptive grid transformation, following this 2D equidistribution principle with the mentioned monitor function $\mathcal{M}$, remains non-singular:

Theorem 1 (For Details of the Proof: [3]) *Let* $\mathcal{M} > 0$, $\mathcal{M} \in C^1(\Omega_c)$ *and* $\mathcal{M}_\xi, \mathcal{M}_\eta \in C^\gamma(\bar{\Omega}_c)$ *for* $\gamma \in (0,1)$. *Then there exists a unique solution* $(x, z) \in C^2(\bar{\Omega}_c)$, *which is a bijection from* $\bar{\Omega}_c$ *into itself. Moreover, the determinant of the Jacobian* $\mathcal{J}$ *satisfies*

$$\mathcal{J} = x_\xi z_\eta - x_\eta z_\xi > 0.$$

Some important ingredients of their proof include the Jordan curve theorem, the Carleman-Hartman-Wintner theorem and the maximum principle for elliptic PDEs.

In reference [1] a deep analysis of the invertibility of more general, so-called σ-harmonic, mappings is given. The transformed PDE model is spatially discretized uniformly in the ξ and η coordinates. For the numerical time-integration of the transformed 2D non-equilibrium PDE and the adaptive grid equations, we have used an IMplicitEXplicit-approach [12, 17]. As an example, the diffusion term (14) is numerically approximated as follows:

$$\begin{aligned}
&(\mathcal{D}(S)S_x)_x|_{i,j}^n \\
&\approx \frac{1}{\mathcal{J}_{i,j}^n}\left[\frac{C_1|_{i+1,j}^n + C_1|_{i,j}^n}{2}\frac{S_{i+1,j}^{n+1} - S_{i,j}^{n+1}}{(\Delta\xi)^2} - \frac{C_1|_{i,j}^n + C_1|_{i-1,j}^n}{2}\frac{S_{i,j}^{n+1} - S_{i-1,j}^{n+1}}{(\Delta\xi)^2}\right. \\
&\quad - C_2|_{i+1,j}^n \frac{S_{i+1,j+1}^{n+1} - S_{i+1,j-1}^{n+1}}{4\Delta\xi\Delta\eta} + C_2|_{i-1,j}^n \frac{S_{i-1,j+1}^{n+1} - S_{i-1,j-1}^{n+1}}{4\Delta\xi\Delta\eta} \\
&\quad - C_2|_{i,j+1}^n \frac{S_{i+1,j+1}^{n+1} - S_{i-1,j+1}^{n+1}}{4\Delta\xi\Delta\eta} + C_2|_{i,j-1}^n \frac{S_{i+1,j-1}^{n+1} - S_{i-1,j-1}^{n+1}}{4\Delta\xi\Delta\eta} \\
&\quad \left. + \frac{C_3|_{i,j+1}^n + C_3|_{i,j}^n}{2}\frac{S_{i,j+1}^{n+1} - S_{i,j}^{n+1}}{(\Delta\eta)^2} - \frac{C_3|_{i,j}^n + C_3|_{i,j-1}^n}{2}\frac{S_{i,j}^{n+1} - S_{i,j-1}^{n+1}}{(\Delta\eta)^2}\right],
\end{aligned} \tag{15}$$

where $C_1 := \frac{1}{\mathcal{J}}\mathcal{D}(S)z_\eta^2$, $C_2 := \frac{1}{\mathcal{J}}\mathcal{D}(S)z_\xi z_\eta$, and $C_3 := \frac{1}{\mathcal{J}}\mathcal{D}(S)z_\xi^2$, respectively. Instead of the 'smart' smoothing operators in space and time, as being used in 1D, here, a filter, as in [18, 23], on the monitor function is applied several times in each time step in the following way:

$$\begin{aligned}
\tilde{\mathcal{M}}_{i,j} = \frac{1}{4}\mathcal{M}_{i,j} &+ \frac{1}{8}\left[\mathcal{M}_{i-1,j} + \mathcal{M}_{i+1,j} + \mathcal{M}_{i,j-1} + \mathcal{M}_{i,j+1}\right] \\
&+ \frac{1}{16}\left[\mathcal{M}_{i-1,j-1} + \mathcal{M}_{i+1,j-1} + \mathcal{M}_{i-1,j+1} + \mathcal{M}_{i+1,j+1}\right].
\end{aligned} \tag{16}$$

This modification yields even smoother grid distributions and enhances the time-integration process as well.

3.3 *Numerical Results*

To support the main results of the analysis in Sect. 3.1, we perform some numerical experiments for the 2D model. The spatial domain is defined by the rectangle $[0, 10] \times [0, 60]$ and the initial solution is a 'tanh'-type function as in 1D, but now situated around the value $z = 55$. We add a small periodic perturbation with frequency ω to test the stability of the two-dimensional waves. The numerical experiments, unless specified differently, make use of a spatial grid with 41×121 grid points.

Figure 5 indeed confirms and illustrates the stability analysis by Egorov et al. [6] and Nieber et al. [15], also briefly described in Sect. 3.1. The left panel shows the numerically calculated growth factor k of the perturbation as a function of the initial frequency ω for several values of the non-equilibrium parameter τ, using the adaptive grid method from Sect. 3.2. The right panel is taken from [6] and depicts a very similar dependence of $k(\omega)$.

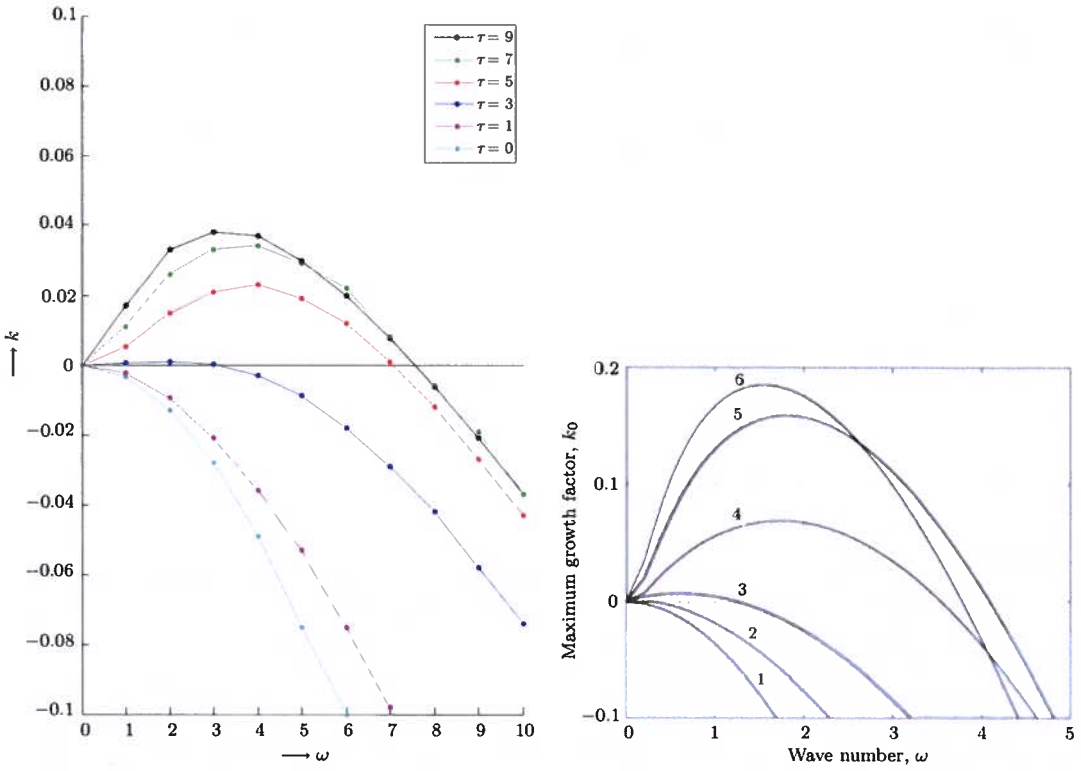

Fig. 5 Left: the growth factor k, numerically determined, as a function of the wave number ω of the perturbation for various values of τ. Right: the theoretical prediction, taken from [6]. Note that the scales on both axes in the two figures are different. The ω on the left is a numerical frequency added to the initial condition, whereas the ω on the right comes from a theoretical analysis. The global behaviour is the same, but the exact values are different. A similar remark holds for the growth factor k

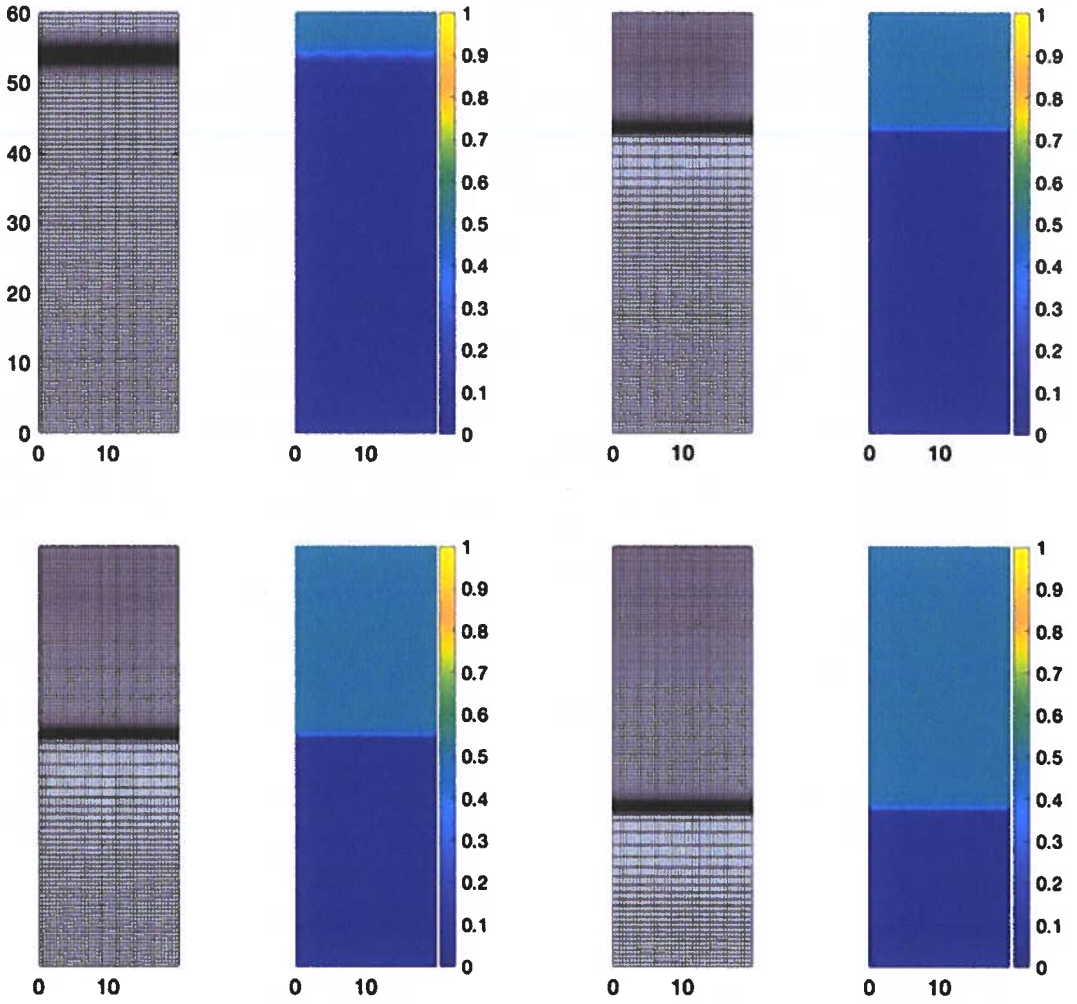

Fig. 6 The water saturation profile and corresponding grid at different times for $\tau = 0$ and $\beta = 0.5$ on a 41×121-grid

In Fig. 6 we show a *stable* travelling wave in two dimensions for $\tau = 0$, $\alpha = 3$ and $\beta = 0.5$: the initial perturbation disappears quickly and the adaptive moving grid follows the steep parts of the wave efficiently and accurately. Figure 7 displays close-ups of the adaptive grid for the solutions in Fig. 6.

Next, in Fig. 8 a similar situation is displayed, but now for $\tau = 10$, $\alpha = 3$ and $\beta = 0.5$: the initial perturbation grows in time and the wave becomes *unstable* creating the shape of a 'finger'. Again, the 2D adaptive grid is situated nicely around the steep parts of the irregularly shaped travelling wave. Figure 9 shows close-ups of the adaptive grids for the solutions in Fig. 8.

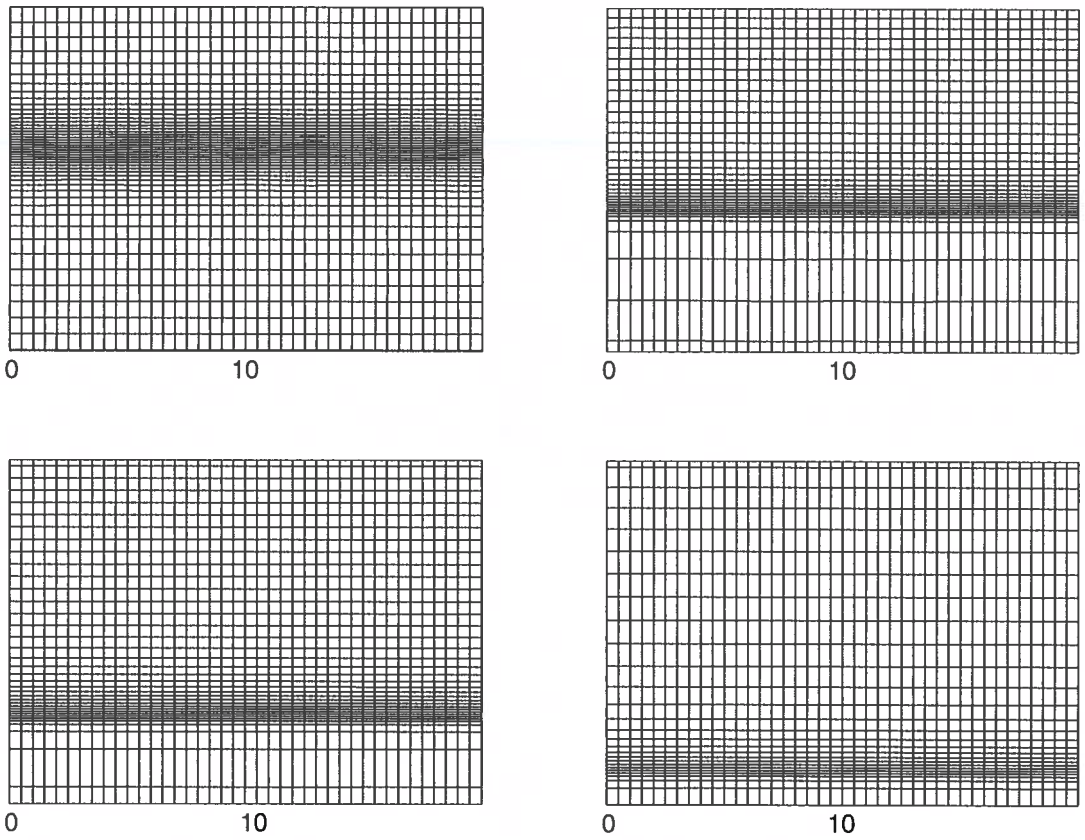

Fig. 7 Close-ups of the adaptive grid near the steep parts of the travelling wave in Fig. 6 at four different points of time for $\tau = 0$ and $\beta = 0.5$

Figure 10 demonstrates the convergence of the adaptive grid solution to an unstable finger with steep transitions. Here, the number of grid points is increased from 21×41 up to 81×241. Note the extra smoothing of the grid distribution. This is due to the time-dependent function $\gamma(t)$ in the monitor function, which becomes more visible for denser grids. Also, it must be mentioned that the non-uniform grid has an important effect of the accuracy of the fingering structure. This phenomenon has also been observed and described in reference [13].

In Fig. 11, the values $\tau = 10$, $\alpha = 3$ and $\beta = 0.2$ are chosen. The smaller value of the parameter β has clearly the effect of producing a more profound fingering structure. Figure 12 shows close-ups of the adaptive grids for these numerical solutions in Fig. 11.

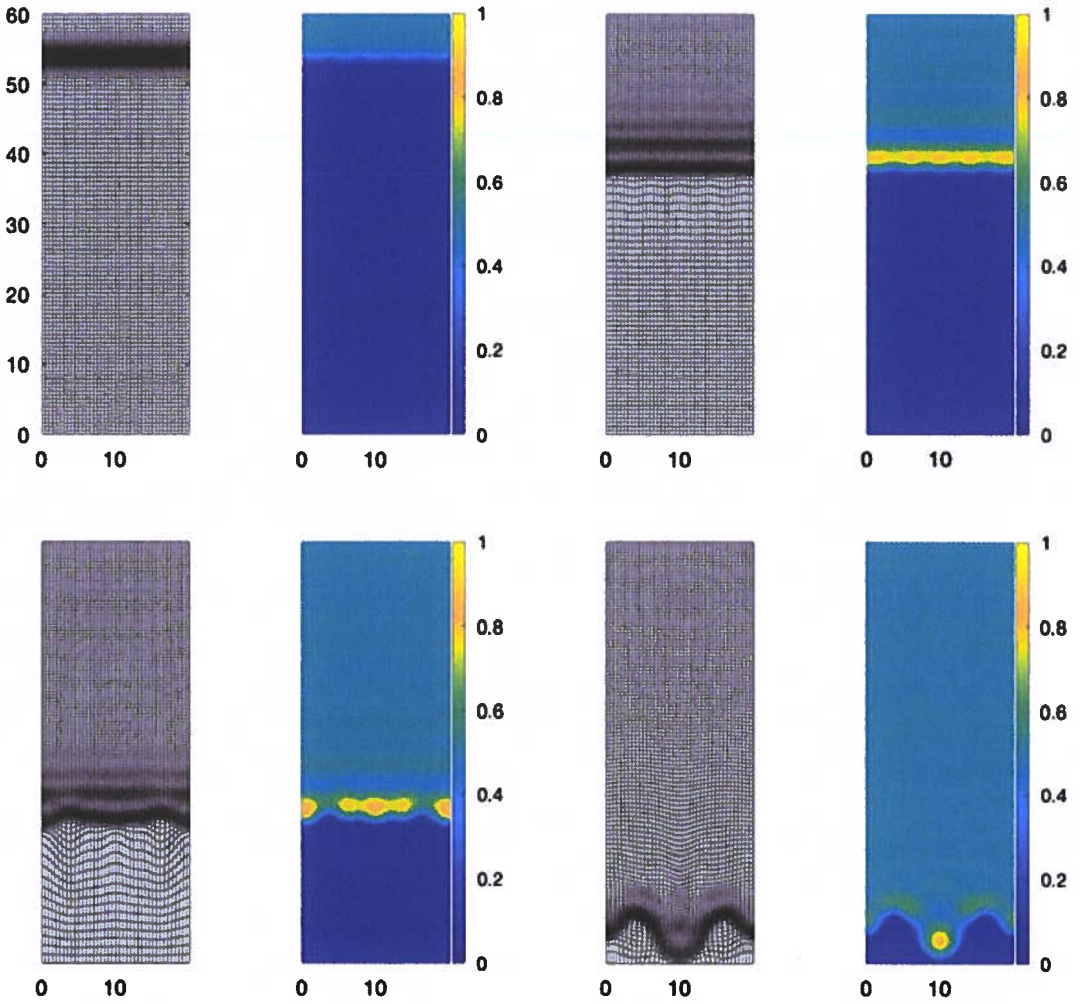

Fig. 8 The water saturation profile and corresponding grid at different times for $\tau = 10$ and $\beta = 0.5$ on a 41×121-grid

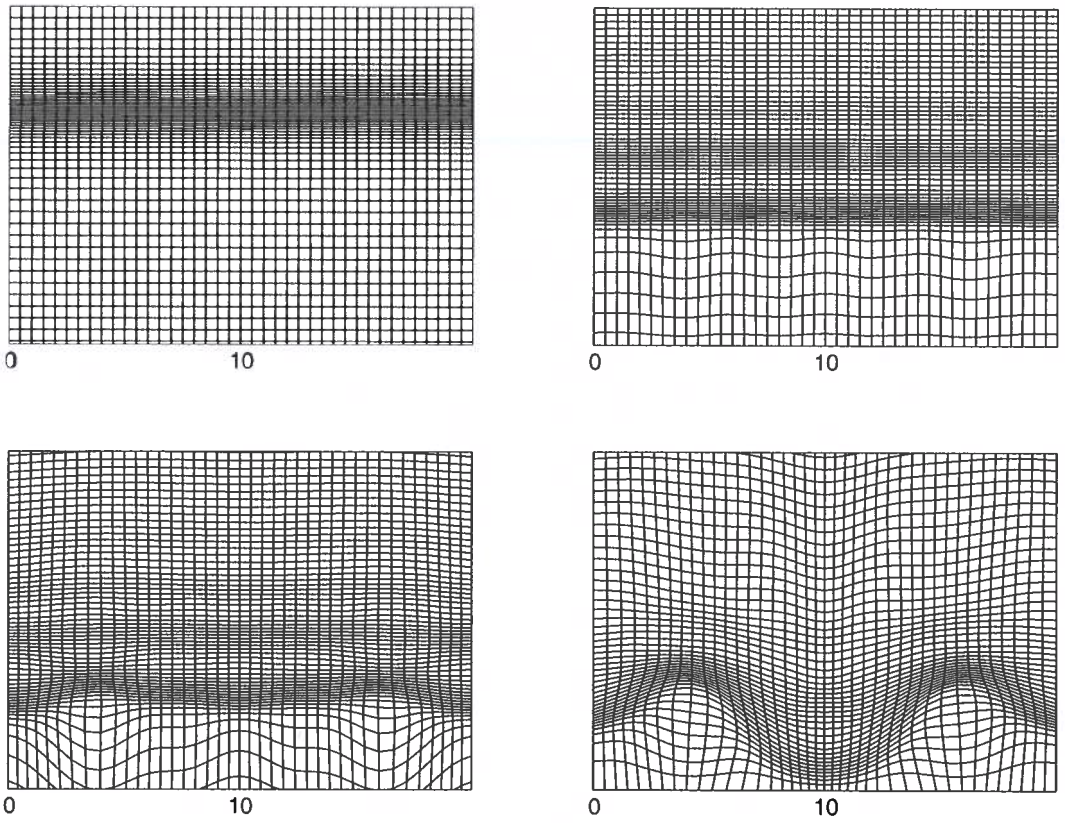

Fig. 9 Close-ups of the adaptive grid near the steep parts of the fingering solution in Fig. 8 for $\tau = 10$ and $\beta = 0.5$

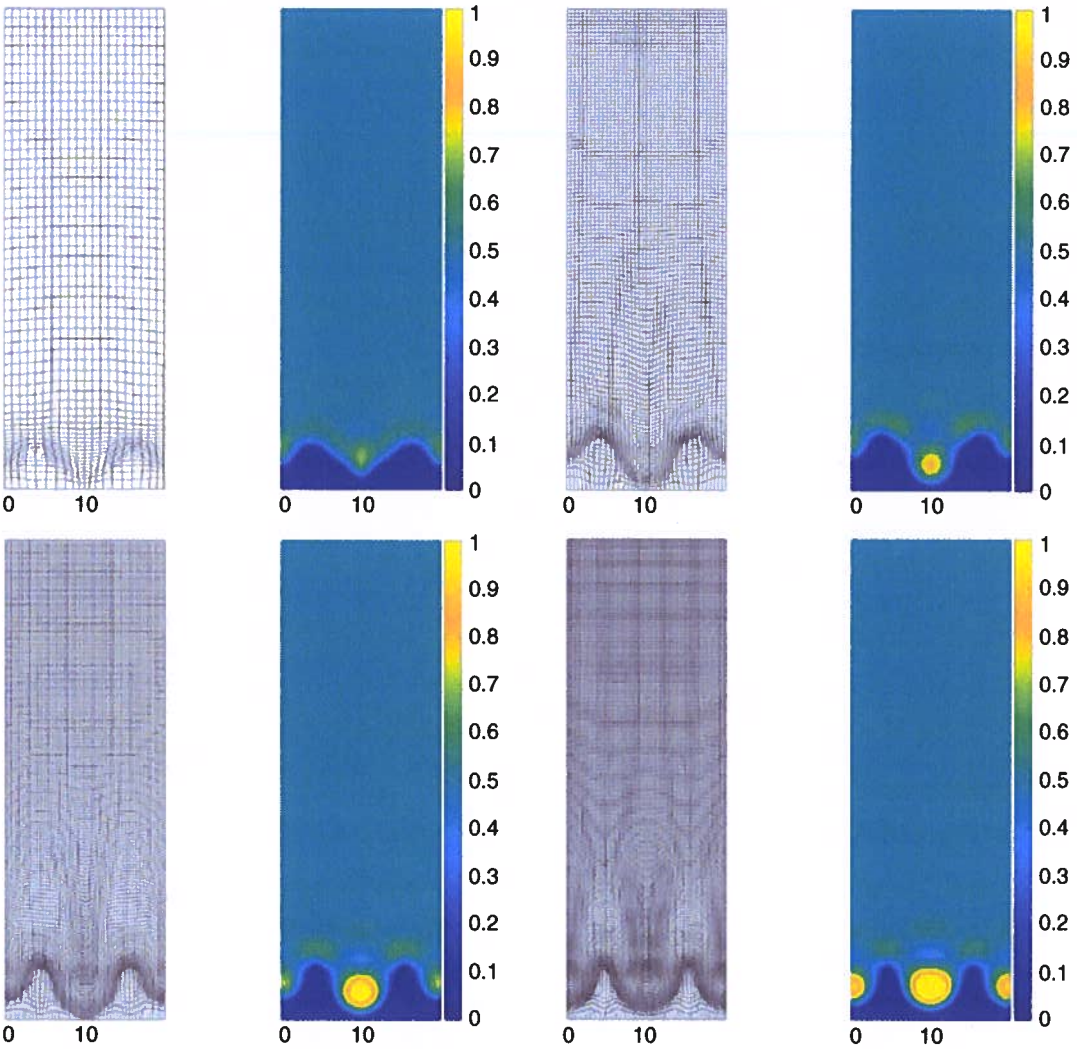

Fig. 10 Adaptive grids and solutions for the case $\tau = 10$ and $\beta = 0.5$ for an increasing number of spatial grid points: 21×61 (top left), 41×121 (top right), 61×181 (bottom left) and 81×241 (bottom right). Note the additional smoothing effect for denser grids of the function $\gamma(t)$ in the monitor function. See also [13] for similar conclusions on the effects of the grid distribution on the fingering structure

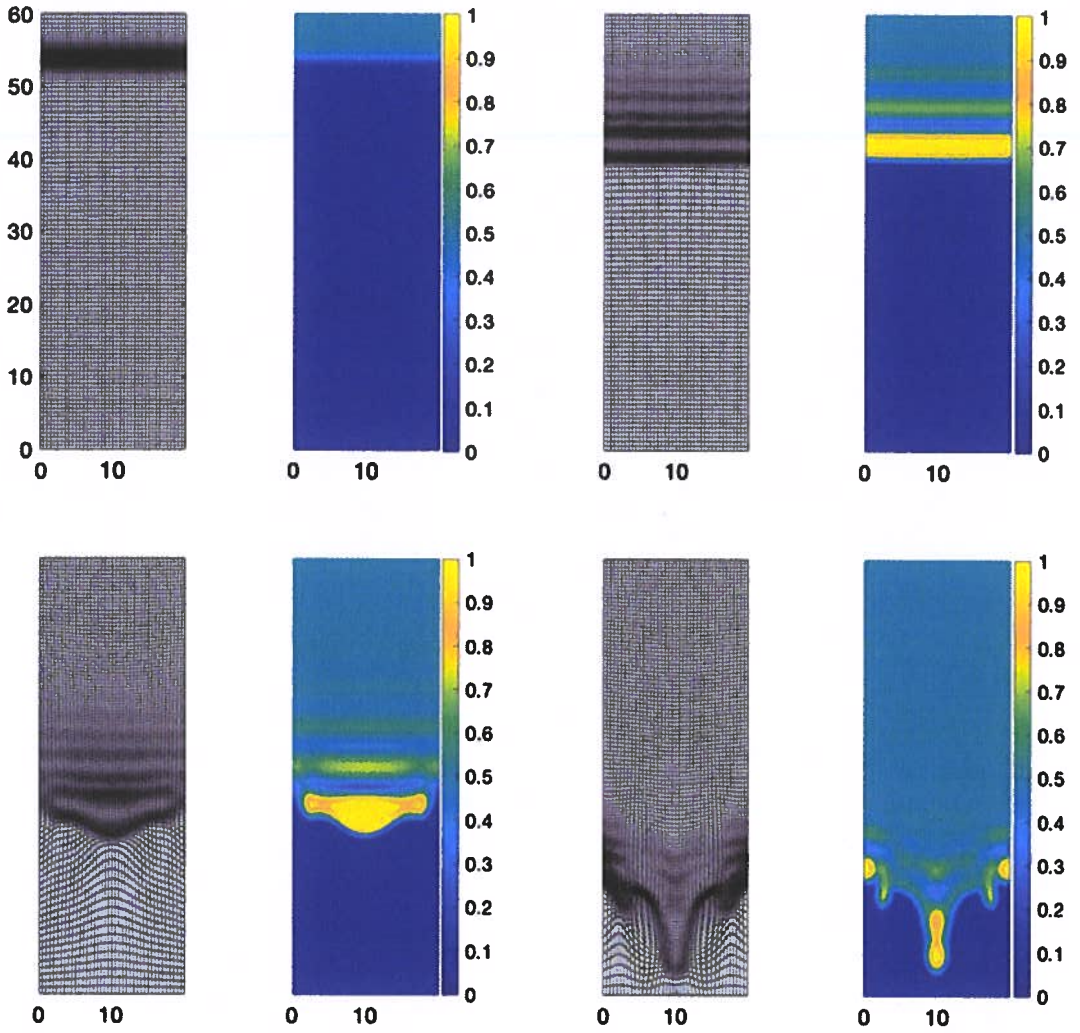

Fig. 11 The water saturation profile and corresponding grid at different times for $\tau = 10$ and $\beta = 0.2$. The instability of the solution, creating a fingering structure, is now more profound than in the previous case. This is due to the smaller value of the parameter β

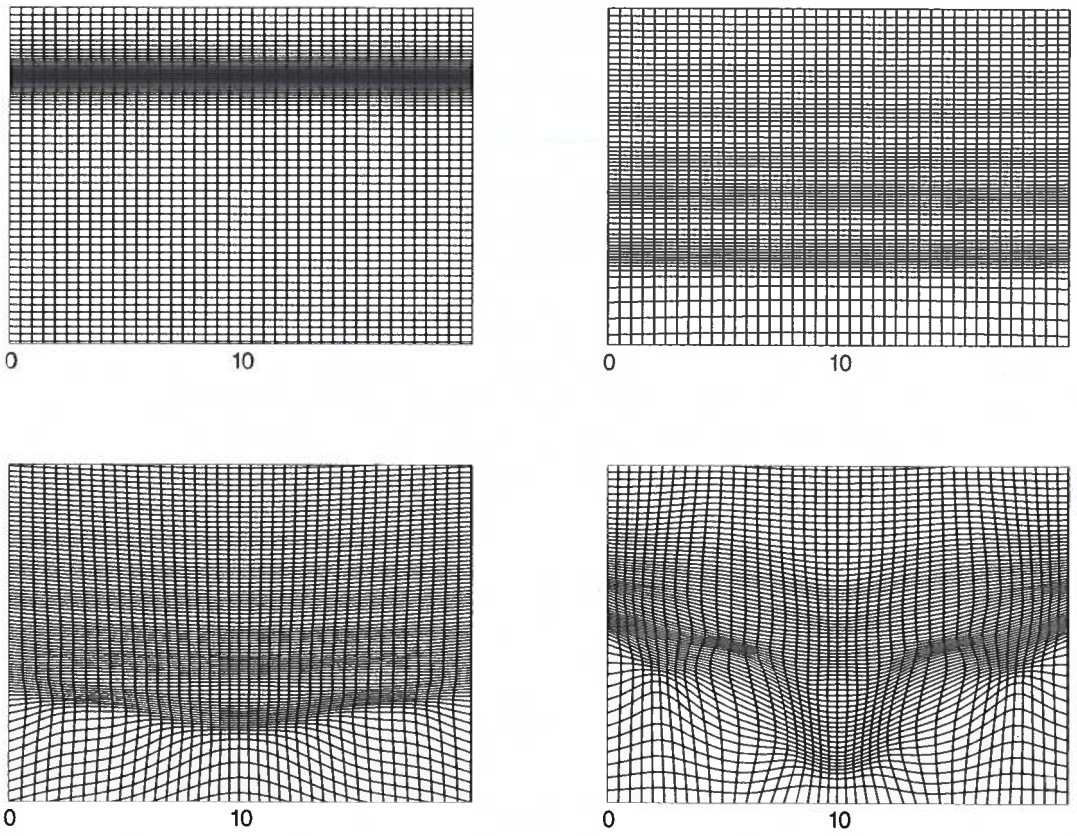

Fig. 12 Close-ups of the adaptive grid near the steep parts of the fingering solution in Fig. 11 for $\tau = 10$ and $\beta = 0.2$

References

1. Alessandrini, G., Nesi, V.: Univalent σ-harmonic mappings. Arch. Rational Mech. Anal. **158**, 155–171 (2001)
2. Budd, C.J., Huang W., Russell R.D.: Adaptivity with moving grids. Acta Numer. **18**, 111–241 (2009)
3. Clement, Ph., Hagmeijer, R., Sweers, G.: On the invertibility of mappings arising in 2D grid generation problems. Numer. Math. **73**(1), 37–52 (1996)
4. Cuesta, C., van Duijn, C.J., Hulshof, J.: Infiltration in porous media with dynamic capillary pressure: travelling waves. Eur. J. Appl. Math **11**, 397 (2000)
5. DiCarlo, D.: Experimental measurements of saturation overshoot on infiltration. Water Resour. Res. **40**, W04215 (2004)
6. Egorov, A.G., Dautov, R.Z., Nieber, J.L., Sheshukov, A.Y.: Stability analysis of gravity-driven infiltrating flow. Water Resour. Res. **39**, 1266 (2003)
7. Hassanizadeh, S.M., Gray, W.G.: Thermodynamic basis of capillary pressure on porous media. Water Resour. Res. **29**, 3389–3405 (1993)
8. Hilfer, R., Doster, F., Zegeling, P.A. Nonmonotone saturation profiles for hydrostatic equilibrium in homogeneous porous media. Vadose Zone J. **11**(3), 201 (2012)
9. Hu, G., Zegeling, P.A.: Simulating finger phenomena in porous media with a moving finite element method. J. Comput. Phys. **230**(8), 3249–3263 (2011)
10. Huang, W., Russell, R.D.: Analysis of moving mesh partial differential equations with spatial smoothing. SIAM J. Numer. Anal. **34**, 1106–1126 (1997)

11. Huang, W., Russell, R.D.: Adaptive Moving Mesh Methods. Springer, New York (2011)
12. Hundsdorfer, W., Verwer, J.: Numerical Solution of Time-Dependent Advection-Diffusion-Reaction Equations. Springer, Berlin (1993)
13. Kampitsis, A.E., Adam, A., Salinas, P., Pain, C.C., Muggeridge, A.H., Jackson, M.D.: Dynamic adaptive mesh optimisation for immiscible viscous fingering. Comput. Geosci. **24**, 1221–1237 (2020)
14. Nicholl, M.J., Glass, R.J.: Infiltration into an analog fracture: experimental observations of gravity-driven fingering. Vadose Zone J. **4**, 1123–1151 (2005)
15. Nieber, J.L., Dautov, R.Z., Egorov, A.G., Sheshukov, A.Y.: Dynamic capillary pressure mechanism for instability in gravity-driven flows; review and extension to very dry conditions. Transp. Porous Media **58**, 147–172 (2005)
16. Petzold, A.G.: A description of DASSL: a differential/algebraic system solver. In: Stepleman, R.S., et al. (eds.) IMACS Trans. Sci. Comput., pp. 65–68. North-Holland, Amsterdam (1983)
17. Ruuth, S.J.: Implicit-explicit methods for reaction-diffusion problems in pattern formation. J. Math. Biol. **34**, 148–176 (1995)
18. Tang, T., Tang, H.: Adaptive mesh methods for one- and two-dimensional hyperbolic conservation laws. SIAM J. Numer. Anal. **41**(2), 487–515 (2003)
19. van Dam, A., Zegeling, P.A.: A robust moving mesh finite volume method applied to 1d hyperbolic conservation laws from magnetohydrodynamics. J. Comput. Phys. **216**, 526–546 (2006)
20. van Dam, A., Zegeling, P.A.: Balanced monitoring of flow phenomena in moving mesh methods. Commun. Comput. Phys. **7**, 138–170 (2010)
21. van Duijn, C.J., Hassanizadeh, S.M., Pop, I.S., Zegeling, P.A.: Non-equilibrium models for two-phase flow in porous media: the occurrence of saturation overshoot. In: Proc. of the 5th Int. Conf. on Appl. of Porous Media, Cluj-Napoca (2013)
22. van Duijn, C.J., Fan, Y., Peletier, L.A., Pop, I.S.: Travelling wave solutions for a degenerate pseudo-parabolic equation modelling two-phase flow in porous media. Nonlinear Anal. Real World Appl. **14**, 1361–1383 (2013)
23. Zegeling, P.A.: On resistive MHD models with adaptive moving meshes. J. Sci. Comput. **24**(2), 263–284 (2005)
24. Zegeling, P.A.: Theory and application of adaptive moving grid methods. In: Adaptive Computations: Theory and Algorithms, pp. 279–332. Science Press, Beijing (2007)
25. Zegeling, P.A., Lagzi, I., Izsak, F.: Transition of Liesegang precipitation systems: simulations with an adaptive grid PDE method. Commun. Comput. Phys. **10**(4), 867–881 (2011)